Light Readout of Small Scintillators Using SiPM Photosensors

Chiara Rita Failla , Simone Amaducci , Gaetano Elio Poma , Paolo Finocchiaro *

Posted Date: 8 September 2025

doi: 10.20944/preprints202509.0685.v1

Keywords: silicon photomultiplier; scintillator; non-linearity

Article

Light Readout of Small Scintillators Using SiPM Photosensors

Chiara Rita Failla [1,2], Simone Amaducci [1], Gaetano Elio Poma [1] and Paolo Finocchiaro [1,*]

[1] INFN - Laboratori Nazionali del Sud - Via S. Sofia 62, 95123 Catania, Italy

[2] Department of Physics and Astronomy - University of Catania - Via S. Sofia 64, 95123 Catania, Italy

* Correspondence: finocchiaro@lns.infn.it

Highlights

Main finding

- Light readout from scintillators by means of SiPM can or cannot give rise to non-linearity at high energy, depending on the light decay time and on the number of SiPM microcells.

Implication

- Careful choice of scintillator and SiPM can prevent or minimize non-linear behavior at high deposited energy.

Abstract

During the last two decades relevant progress has been achieved in silicon photomultiplier (SiPM) technology, so that in an increasing number of radiation detection applications they are proposed as a viable alternative to traditional photomultiplier tubes (PMT). Applications where the light from tiny scintillating crystals is detected by a single SiPM raise the question of the possible non-linearity of the response due to saturation of the number of microcells involved. In other cases where larger scintillators subtend arrays of SiPMs the same question could hold. This work tries to disentangle such a question with a realistic numerical approach and a few tests, showing that possible saturation effects depend on the interplay between the features of the scintillator and of the SiPM (array). The quantitative results of this analysis can likely be used to better plan future radiation detection systems and to highlight their linearity boundaries.

Keywords: silicon photomultiplier; scintillator; non-linearity.

1. Introduction

The detection of gamma rays is one of the most widespread applications in radiation physics worldwide. Whenever high spectroscopic precision is required, in order to identify the emitting radioisotopes, the gold standard of detectors is the germanium semiconductor [1]. In most other cases much less expensive and more practical detectors based on scintillators are exploited. A scintillator detector is based on special organic or inorganic materials exhibiting the notable feature of producing tiny flashes of light when hit by radiation. We will not go into details of how such a light is produced at molecular level, but we just remind here that the produced visible photons are emitted isotropically according to an exponential time distribution with a decay constant μ characteristic of each material. Organic scintillators are typically faster, with μ values even down to 1-2 ns, whereas inorganic crystals span a wide range from tens of nanoseconds even up to milliseconds [2,3].

Throughout several decades the light readout of scintillators has mainly been performed by means of photomultiplier tubes (PMT), until more recently a new kind of solid state photodetector

 doi:10.20944/preprints202509.0685.v1

has come onto the playground, namely the silicon photomultiplier (SiPM). Such a device, suggested many years ago but only recently industrially produced because of relevant technological advances, operates according to a quasi-digital scheme. Indeed, it consists of an array of semiconductor microcells kept in a quiescent state slightly above the breakdown voltage. When a visible photon interacts with one such microcell it triggers a discharge, limited by a built-in quenching resistor, that gives rise to a signal consisting of the electrical charge stored in the microcell itself. Being all microcells identical, each one produces the same signal when hit by a visible photon and then a light pulse consisting of n photons should produce a signal n times as large as the single photon does.

Of course this ideal scheme has several limitations in real sensors:

1. Only a fraction of the photons hitting the SiPM produces signals, because of its photon detection efficiency (PDE) that is far from 100%;
2. When two or more photons interact with the same microcell the produced signal is the same (this is the so called problem of the multiple hit);
3. Each microcell has a recharging dead time, i.e., a short time interval after being triggered, during which it is inactive because its voltage is being restored to the operating value;
4. As the microcells are kept above breakdown, every now and then they can spontaneously discharge for thermal reason, giving rise to an overall poissonian dark noise mainly consisting of single microcell signals plus rarer double, triple and higher order spurious coincidences.

However, the main limitation of SiPMs is their maximum size, that for the currently available devices is 6 mm × 6 mm. Such a small size can also be seen as an advantage, should one be interested to set up a miniature gamma ray detector. Due to the decreasing cost of these photosensors, the size limitation is currently being overcome by arranging arrays of SiPMs for the readout of larger scintillators. Details on the features and operation of SiPMs can be found in [4–7] and in the copious list of references therein.

One of the questions arising from the above mentioned operational limitations is the linearity of the response, in particular when detecting gamma rays of the order of 1-2 MeV [8–11]. In this work we examine the behavior of two different models of SiPM, when coupled to five popular scintillators, as a function of the energy deposited by gamma rays. In Section 2 we describe the algorithm developed to evaluate the behavior of a SiPM illuminated by scintillation light, and in Section 3 we show the results obtained with the several examined combinations of scintillator + SiPM along with the experimental results obtained in two particular real cases. Finally, in Section 4 we discuss the relevant take-home messages arising from our results.

2. Materials and Methods

2.1. Detecting Gamma Rays

The interaction of gamma rays with matter occurs according to three main processes:

- Photoelectric effect, dominating at low energy, when the gamma disappears transferring all of its energy to an electron;
- Compton scattering, dominating at intermediate energy, with the gamma scattering off an electron and imparting it some kinetic energy;
- e+e- pair creation close to a nucleus, exploiting 1.022 MeV of the incoming gamma thus being the dominating effect at very high energy.

For the low to medium energy range considered here, namely up to ≈ 2 MeV, only photoelectric effect and Compton scattering are relevant. The energetic electron thus produced interacts with other electrons and gives rise to a so called shower, i.e., a cloud of energetic electrons whose total kinetic energy is equal to the energy released by the initial gamma interaction. The scintillation light in scintillators is produced by the interaction of these energetic electrons with "color centers", i.e., typically dopants in the material capable to reach an excited level by collision which deexcites by emitting visible light. The number of visible photons produced in each gamma interaction is generally

 doi:10.20944/preprints202509.0685.v1

proportional to the energy deposited by the gamma ray into the material. The detection and energy measurement of the gamma rays is done by measuring the amount of scintillation light produced by means of some photodetector which converts light into an electric signal. Due to the very small amount of light produced a physical amplification is quite often required, and the task is accomplished by using a photomultiplier device.

Different scintillators have different linearity between deposited energy and scintillation light, especially at high deposited energy where some saturation of the light yield could be expected. Saturation can also be expected due to the employed photosensor, especially in the case of photoelectric interaction when the full gamma energy is transferred to the material. Starting from our previous experience with detectors based on scintillators and SiPMs [12–15], we examined five popular scintillation materials, whose main features relevant for this study are listed in Table 1 [16], and their response when coupled to two models of 6 mm × 6 mm SiPM [17,18] whose features are listed in Table 2.

Table 1. Main features, relevant to this study, of the selected five popular scintillators.

	CsI(Tl)	**LaBr3(Ce)**	**CeBr3**	**BGO**	**NaI(Tl)**
Light yield [photons/keV]	60	70	70	10	45
Decay time [ns]	960	30	20	300	250
Emission spectrum from ref.	[19]	[20]	[21]	[22]	[23]
Refractive index at λ max	1.8	1.9	2.1	2.1	1.8
Weighted PDE SensL [%]	27%	31%	34%	29%	35%
Weighted PDE Hamamatsu [%]	41%	42%	45%	44%	48%

Table 2. Main features, relevant to this study, of the two selected SiPMs.

	MICROFC–60035–SMT SensL (now OnSemi) [17]	**S14160-6050HS Hamamatsu** [18]
number of microcells	18980	14331
microcell recharge time [ns]	100	92

2.2. Collecting the Scintillation Light

The number of scintillation photons collected on the photosensor depend on the geometric features of the detector and, more important, on the type and quality of the outer surface of the scintillator. Indeed, a bare scintillator would lose most of the light through its outer faces, and basically collecting only those photons traveling straight from the emission point to the photosensor. This is why scintillators are generally coated with a highly reflective layer (paint, resin, ...) to maximize the light collection efficiency allowing photons to be collected also after several internal reflections. The reflector is not specular but white so that, contrary to the case of geometrical reflection, the light path inside the scintillator is quickly randomized. This way any possible variation of the light collection efficiency with its emission position inside the scintillator is minimized. The typical reflectivity values of the employed reflector materials range from 0.9 to 0.96.

Two detector geometries have been examined, representative of two major possible approaches to the spectroscopic detection of gamma rays with scintillators and SiPMs. The first one concerns applications as miniature detectors and dosimeters, whereas the second has crystal size and shape typical of several existing commercial products:

- A compact configuration with a 1 cm × 1 cm × 1 cm scintillator coupled to a single 6 mm × 6 mm SiPM (Figure 1a);
- A bigger one with a cylindrical scintillator of 3.81 cm diameter and 3.81 cm height (1.5" × 1.5") coupled to a square array of 4 × 4 SiPMs (Figure 1b).

 doi:10.20944/preprints202509.0685.v1

The results and considerations that we are going to describe in the following can be easily rescaled to similar geometrical configurations with larger or smaller scintillators and different number of SiPMs.

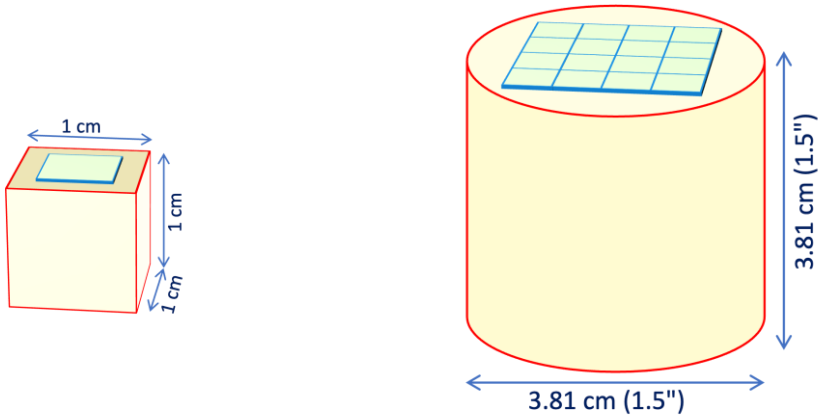

(**a**) (**b**)

Figure 1. The two detector geometries studied: (**a**) 1 cm × 1 cm × 1 cm scintillator coupled to a single 6 mm × 6 mm SiPM; (**b**) cylindrical scintillator of 3.81 cm diameter and 3.81 cm height coupled to a square array of 4 × 4 SiPMs.

Due to the compact size of both geometries with respect to the (re)absorption length of several tens of centimeters for all of the scintillators under consideration, in this study we decided to neglect the possible self-absorption of scintillation photons in the scintillator material. The light collection efficiency, i.e., the fraction of photons reaching the SiPM, was first estimated by means of a simple naive approach:

- No real geometry is considered for the system and no light propagation is implemented;
- A scintillation photon produced somewhere inside the crystal reaches a point on the inner surface;
- We assume it can hit the SiPM with a probability ε roughly equal to the ratio between the area of the SiPM and the total area of the crystal;
- Otherwise it can be reflected or absorbed with probability r and $(1-r)$ respectively, being r the reflectivity of the inner surface.
- We denote with $P_1 = \varepsilon$ the probability that the photon is collected directly on the first step, with P_2 the probability that the photon is collected after one reflection (i.e., at the second step), and so on;
- After each step the probability of the photon to be still available is $(1-\varepsilon)r$ (i.e., not collected and reflected), whereas the probability to be collected at the following step is still ε.
- The sum of all the probabilities of collection in any number of steps, thus regardless of the number of reflections, represents the light collection efficiency (Eq.1).

This calculation was done for several values of the reflectivity ranging from 0.9 to 1, with the elementary collection probabilities $\varepsilon = 0.06$ and $\varepsilon = 0.084$ given by the area ratios for the cases of Figure 1a,b.

$$\begin{aligned} P_1 &= \varepsilon \\ P_2 &= \varepsilon(1-\varepsilon)r \\ P_3 &= \varepsilon[(1-\varepsilon)r]^2 \\ &\dots \\ P_n &= \varepsilon[(1-\varepsilon)r]^{n-1} \end{aligned} \tag{1}$$

 doi:10.20944/preprints202509.0685.v1

$$P = \sum_n P_n = \sum_n \varepsilon[(1-\varepsilon)r]^{n-1} = \varepsilon \frac{1-[(1-\varepsilon)r]^n}{1-(1-\varepsilon)r} \approx \frac{\varepsilon}{1-r+r\varepsilon}$$

In order to support or disprove these results we performed a set of more sophisticated Monte Carlo simulation runs by means of Geant4 [24]. The inner surfaces of the scintillator were assumed to produce diffuse Lambertian reflection [25], each run with a different value of the reflectivity. Inside the crystal we generated randomly 10^5 scintillation photons per run, following each one throughout its path and reflections until being absorbed in a wall or reaching the photosensor. The two geometries of Figure 1 were implemented and eleven runs per configuration were performed, with the reflectivity of the walls ranging from 0.9 to 1 in steps of 0.1. The runs with reflectivity equal to one showed that the average time for the detection is 0.62 ns and 1.6 ns respectively, which assuming a refractive index around 1.9 correspond to average path lengths of the order of 10 and 25 cm. In case of reflectivity equal to 0.95 these values roughly halve to about 5.5 and 13 cm, much smaller than the attenuation length values in the considered crystals, thus justifying the choice of neglecting the self-absorption.

The resulting values of the light collection efficiency for the two approaches and for the two detector geometries are plotted in Figure 2. Surprisingly, the differences between the simple and the Monte Carlo approaches are quite small thus suggesting that the simple formula of Eq.1 can realistically be used for future evaluations of similar configurations. Curiously, we also found empirically that if one increases the ε value for both geometries to $\varepsilon+ = \varepsilon \times 1.067$, thus obtaining $\varepsilon+ = 0.064$ and $\varepsilon+ = 0.090$, the two approaches would become equal well below the percent level, and this holds for both geometrical configurations. This aspect could perhaps be worth future additional investigation. The ratio between simple and Geant4 values is plotted in Figure 3 for the cube and the cylinder geometries. Also plotted are the same ratios for the cases of empirically increased ε values. The data of Figures 2 and 3 are also listed in Table A1 and Table A2 of Appendix A. However, for all of the following calculations we decided to use the light collection efficiency values of $P \approx 0.56$ and $P \approx 0.65$ resulting from Eq.1 for cube and cylinder geometries respectively, choosing a reflectivity value of $r \approx 0.95$ and the above mentioned elementary collection probabilities $\varepsilon = 0.06$ and $\varepsilon = 0.084$.

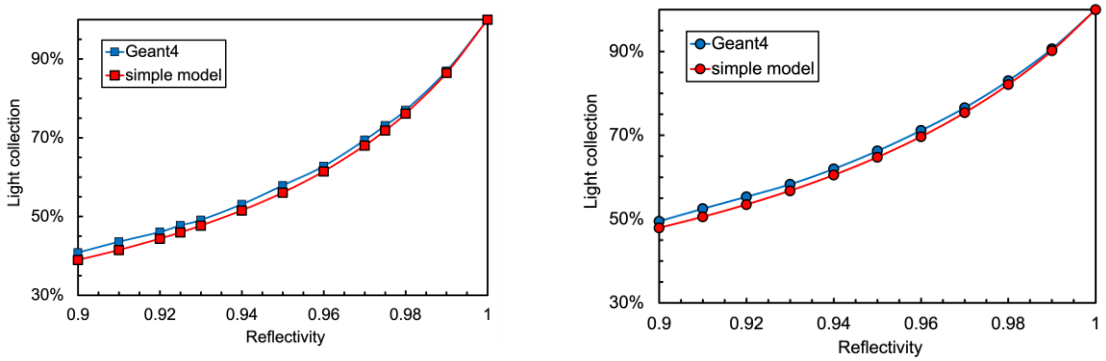

Figure 2. Simulation of the light collection efficiency as a function of the reflectivity of the walls: (**a**) for the cubic configuration of Figure 1a; (**b**) for the cylindrical configuration of Figure 1b.

 doi:10.20944/preprints202509.0685.v1

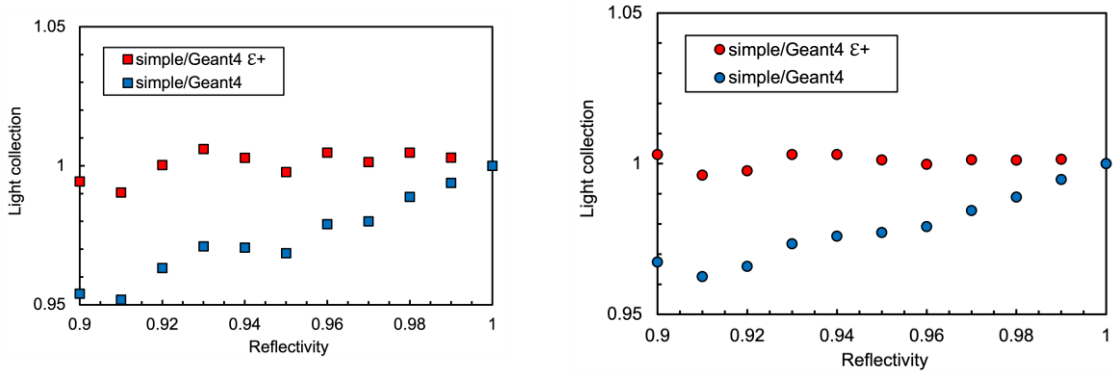

Figure 3. Ratio simple-to-Geant4 between the curves of Figure 2: (**a**) Cubic configuration, also shown is the case of the empirically increased ε value. (**b**) Cylindrical configuration, also shown is the case of the empirically increased ε value.

2.3. Detecting the Collected Light

The physical quantities to be considered for the detection with SiPMs are the light yield of the crystal, the light decay time, the emission spectrum, the collection efficiency of the chosen detector geometry, the SiPM's PDE, its number of microcells, the microcell recharge time (i.e., dead time). If we want to calculate the expected response of the photosensor we have to take into account all these quantities at the same time. We used the values listed on Table 1 and Table 2, and in order to show the behavior of the decay time in real operation we plotted in Figure 4 a signal waveform acquired from a CsI(Tl) scintillator coupled to a SensL SiPM in the configuration of Figure 1a with a digital scope. An exponential fit to the waveform produces a decay constant $\mu = 0.96$ μs as expected.

As for the PDE, we multiplied the PDE(λ) function of each SiPM [17,18] by the light emission spectra of the five scintillators [19–23] (Figure 5) normalized to unit area. The integral of such a convolution represents the effective PDE of each SiPM when detecting the light emitted by each scintillator. The resulting values are reported in Figure 6.

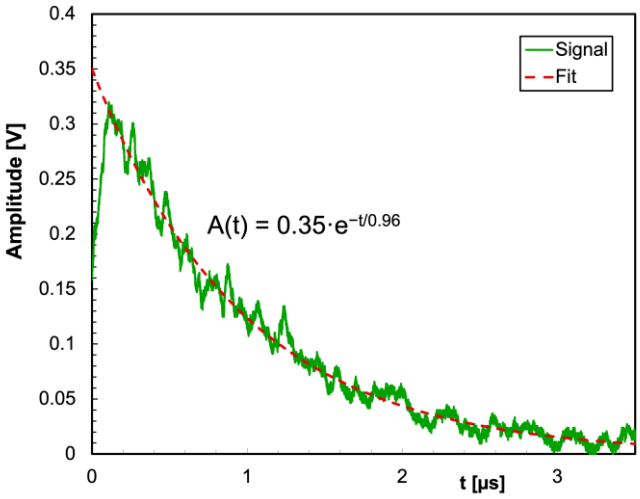

Figure 4. Example of a signal waveform acquired from a CsI(Tl) scintillator coupled to a SensL SiPM in the configuration of Figure 1a with a digital scope. The exponential fit to the waveform has a decay constant of 0.96 μs as expected.

Preprints.org (www.preprints.org) | NOT PEER-REVIEWED | Posted: 8 September 2025 doi:10.20944/preprints202509.0685.v1

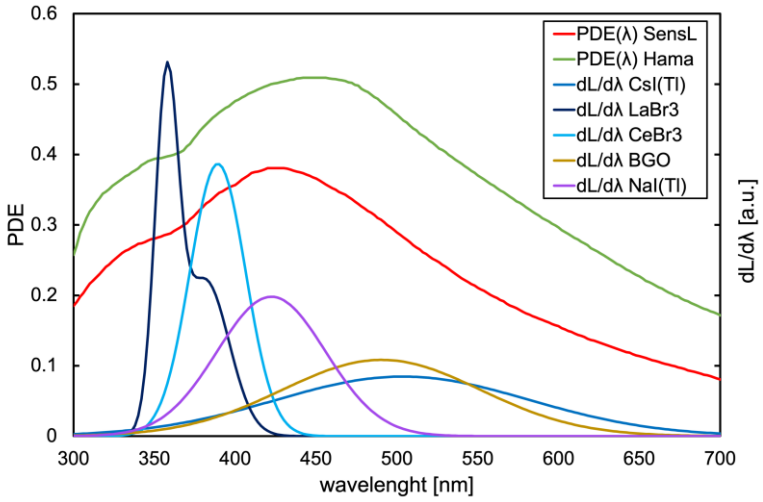

Figure 5. The photon detection efficiency of the two SiPMs [17,18] (left scale), and the light emission spectra of the five scintillators normalized to unit area [19–23] (right scale).

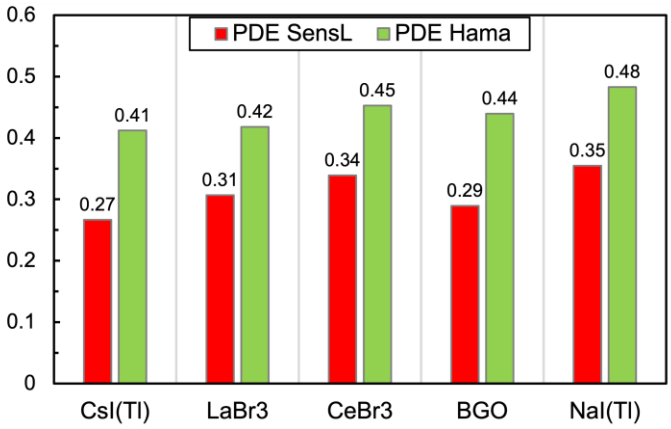

Figure 6. Effective PDE of the two SiPMs when detecting the light emitted by each scintillator, calculate by integrating the product of the PDE(λ) function with the light emission spectrum.

There are two different mechanisms possibly leading to loss of linearity in a SiPM: (i) signal saturation due to multiple photons interacting with the same microcell but being detected as one; (ii) loss of photons due to microcells hit during their recharge dead time because of a previous hit. The number of microcells actually fired by a bunch of photons can be smaller than the number of electron avalanches generated in the SiPM, because two or more avalanches generated in the same microcell produce the same signal and thus are seen as one. The most probable number of microcells *f(q)* actually triggered (i.e., when a photoelectron is produced capable of producing an avalanche) by a bunch of q photons impinging randomly on a SiPM with m microcells and PDE equal to p can be evaluated based on the binomial distribution.

- $\frac{p}{m}$ is the probability for a single microcell to be triggered by one impinging photon;
- $\left(1-\frac{p}{m}\right)$ is the probability that a single microcell is not triggered by one impinging photon;
- $\left(1-\frac{p}{m}\right)^q$ is the probability that a single microcell is not triggered by q impinging photons;
- $\left[1-\left(1-\frac{p}{m}\right)^q\right]$ is the probability that a single microcell is triggered by at least one of the q impinging photons.

As there are m microcells the expected number of triggered ones is

$$f(q) = m\left[1-\left(1-\frac{p}{m}\right)^q\right] \quad (2)$$

By exploiting the notable limit shown below

 doi:10.20944/preprints202509.0685.v1

$$\lim_{n\to\infty}\left(1+\frac{x}{n}\right)^{n}=e^{x} \tag{3}$$

one obtains the much simpler approximate formula

$$f(q)=m\left(1-e^{-\frac{pq}{m}}\right). \tag{4}$$

The effect of the possible loss due to dead time of recharging microcells requires to consider the time development of the light pulse. Therefore we developed a simple algorithm that considers the production of photons exponentially decreasing in time with the decay constant of the scintillator, using time slots of *5 ns*. In each time slot the number of triggered microcells is calculated by means of Eq.4, using a variable number of available microcells m calculated on the basis of the number of previously triggered ones and of their recharge time which makes them temporarily unavailable. The algorithm follows the light pulses during few microseconds, that is much longer than the slowest decay constant of the considered scintillators, and calculates the sum of all the numbers of triggered microcells that is proportional to the integral of the output signal.

3. Results

The combination of the light decay constant of the scintillator with the microcell recharge time of the SiPM produces an initial decrease of the number of available microcells that could or could not influence significantly the linearity of the SiPM response, depending on the deposited energy, on the scintillator type, and on the total number of microcells. In Figure 7a we show as an example the number of triggered and of available microcells as a function of time, for the case of 2 MeV deposited in a 1 cm × 1 cm × 1 cm CsI(Tl) crystal read by the SensL SiPM. Also shown is the ideal number of microcells that would be triggered if no recharge dead time were present. In Figure 7b we plotted the ratio between the number of fired microcells to the ideal one as a function of time. It can be seen that in this case the initial decrease in the number of available microcells does not influence the overall linear response, as there is no appreciable difference between the ideal and the effective total numbers of triggered cells. Figure 8 shows the corresponding plots for the case of the same scintillator coupled to the Hamamatsu SiPM. Even in this case the response is basically linear, even though the non-linearity is slightly larger to due to the smaller number of microcells. Figures 9–16 show the similar plots for all the other combinations of scintillator and SiPM listed in Table 1 and Table 2 respectively. It can be immediately observed that LaBr3(Ce) and CeBr3 give rise to an enormous non-linearity due to the large amount of scintillation photons reaching the SiPM in a very short time interval, thus totally blinding it for a while and losing a considerable fraction of the light signal. In Figure 17 we summarize the results from Figures 7–16 by integrating the plots over time: (a) the total number of ideal hits and of actually triggered microcells for all the examined configurations of scintillator and SiPM; (b) the expected non-linearity i.e., 1−(triggered/ideal).

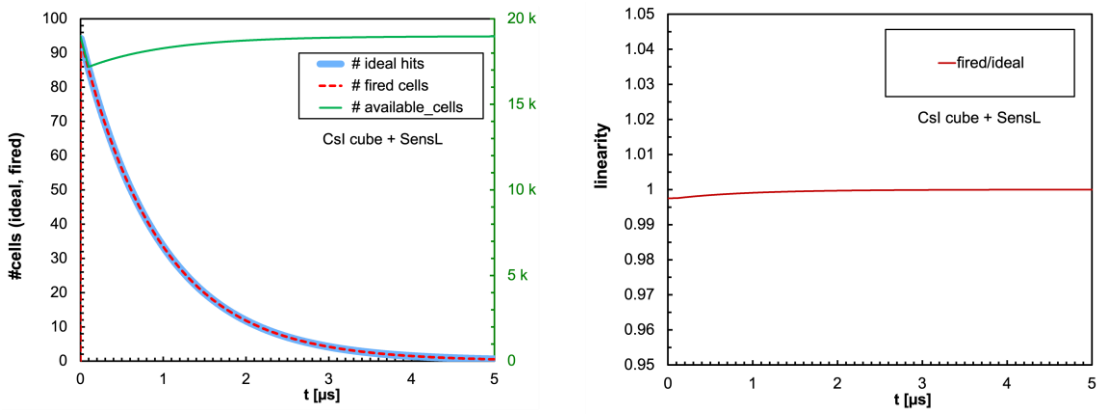

(**a**) (**b**)

Preprints.org (www.preprints.org) | NOT PEER-REVIEWED | Posted: 8 September 2025 doi:10.20944/preprints202509.0685.v1

Figure 7. (**a**) Time evolution of the number of triggered (dashed red line) and of available (green line, right-hand scale) microcells, for the case of 2 MeV deposited in a 1 cm × 1 cm × 1 cm CsI(Tl) crystal read by the SensL SiPM. The time step is 5 ns. Also shown is the ideal number of microcells (light blue line) that would be triggered if no recharge dead time were present. (**b**) Ratio between the number of fired microcells to the ideal one as a function of time.

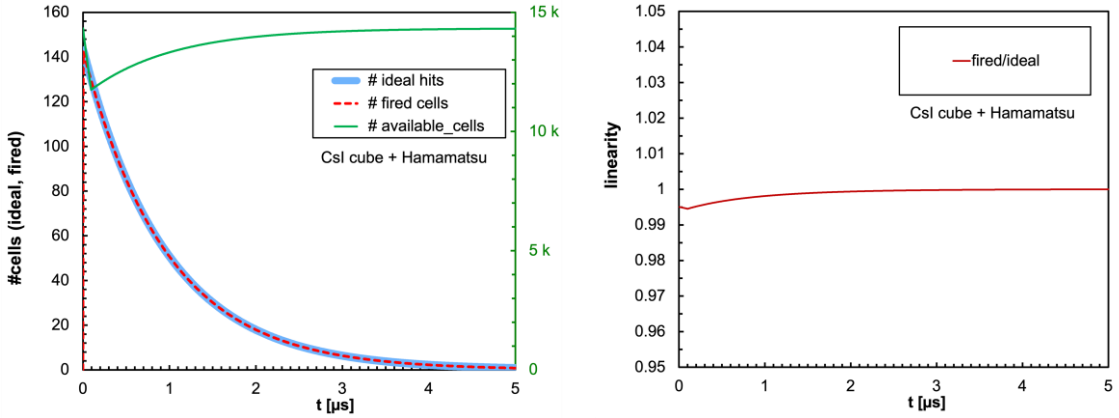

(**a**) (**b**)

Figure 8. (**a**) Same plot as in Figure 7a with the CsI(Tl) cubic crystal coupled to the Hamamatsu SiPM. (**b**) Same plot as in Figure 7b.

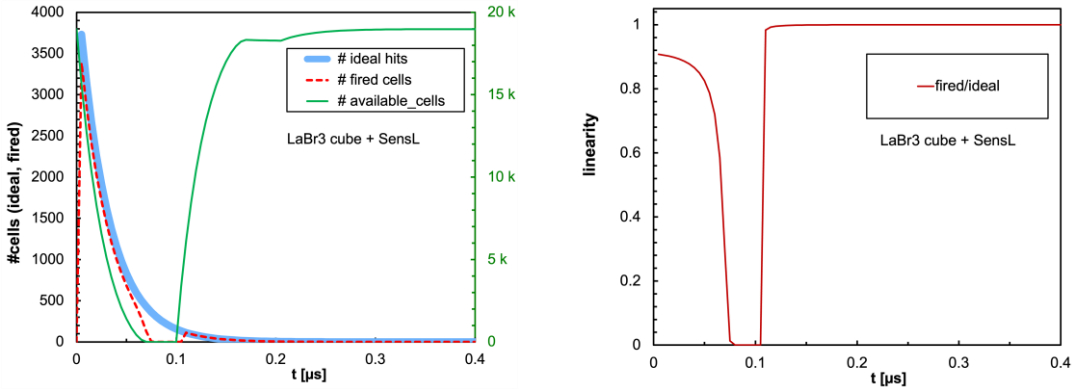

(**a**) (**b**)

Figure 9. (**a**) Same plot as in Figure 7a with the LaBr3(Ce) cubic crystal coupled to the SensL SiPM. (**b**) Same plot as in Figure 7b.

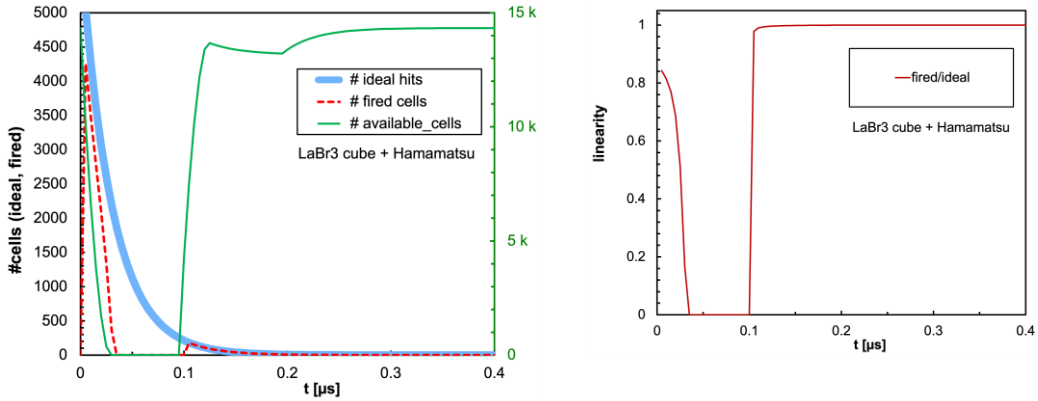

 doi:10.20944/preprints202509.0685.v1

(**a**) (**b**)

Figure 10. (**a**) Same plot as in Figure 7a with the LaBr3(Ce) cubic crystal coupled to the Hamamatsu SiPM. (**b**) Same plot as in Figure 7b.

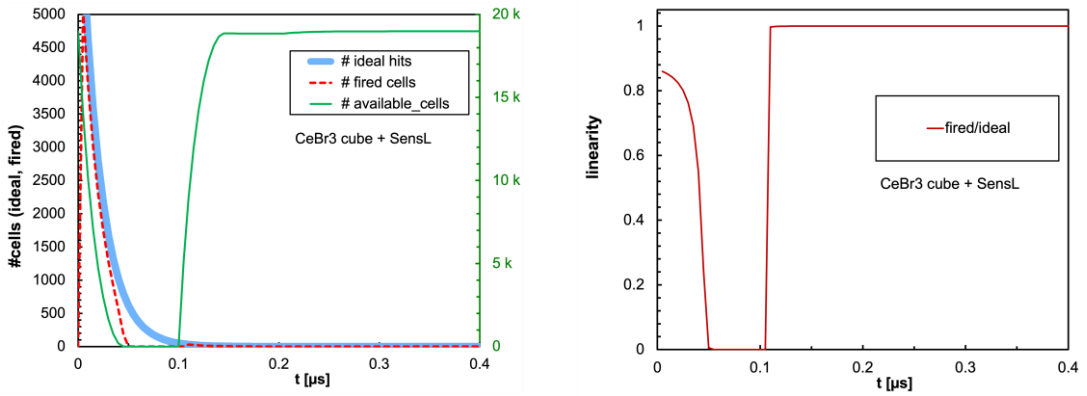

(**a**) (**b**)

Figure 11. (**a**) Same plot as in Figure 7a with the CeBr3 cubic crystal coupled to the SensL SiPM. (**b**) Same plot as in Figure 7b.

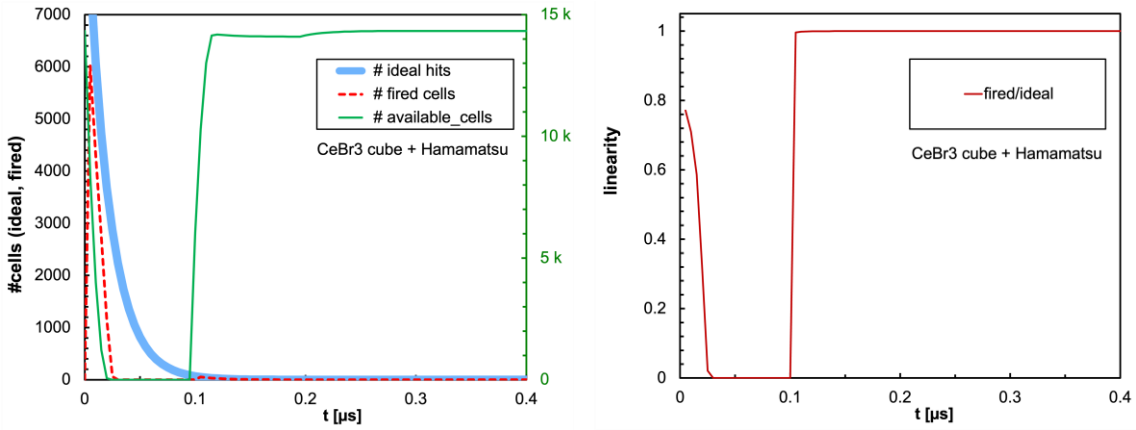

(**a**) (**b**)

Figure 12. (**a**) Same plot as in Figure 7a with the CeBr3 cubic crystal coupled to the Hamamatsu SiPM. (**b**) Same plot as in Figure 7b.

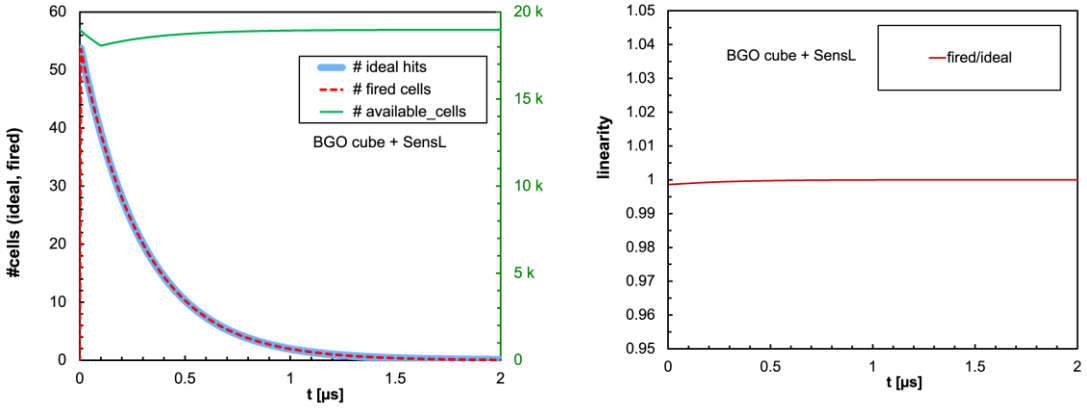

(**a**) (**b**)

 doi:10.20944/preprints202509.0685.v1

Figure 13. (**a**) Same plot as in Figure 7a with the BGO cubic crystal coupled to the SensL SiPM. (**b**) Same plot as in Figure 7b.

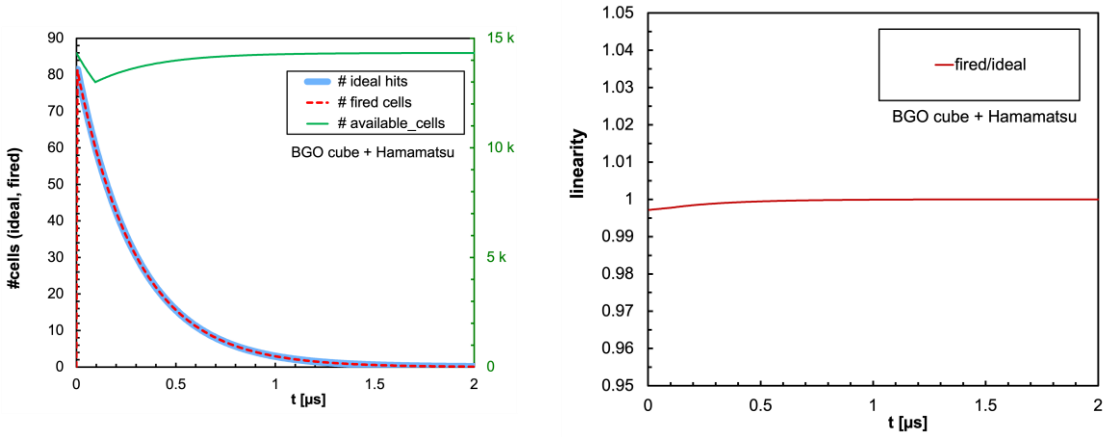

(**a**) (**b**)

Figure 14. (**a**) Same plot as in Figure 7a with the BGO cubic crystal coupled to the Hamamatsu SiPM. (**b**) Same plot as in Figure 7b.

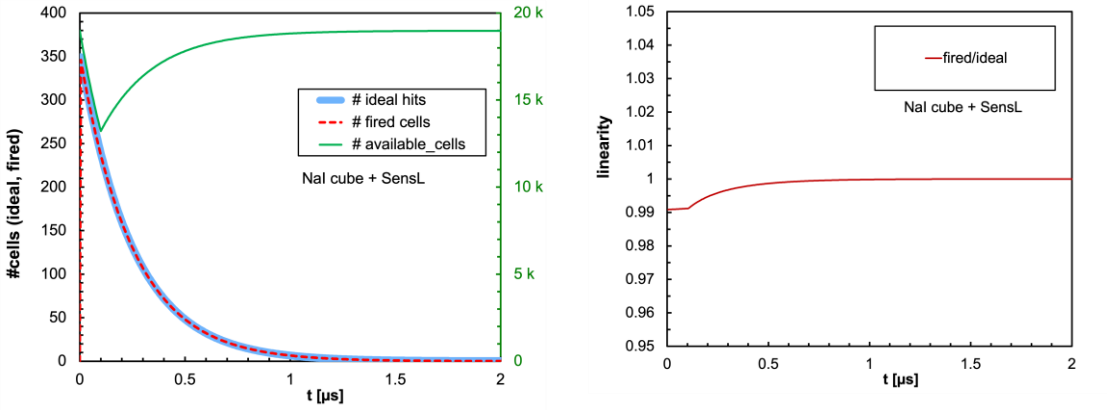

(**a**) (**b**)

Figure 15. (**a**) Same plot as in Figure 7a with the NaI cubic crystal coupled to the SensL SiPM. (**b**) Same plot as in Figure 7b.

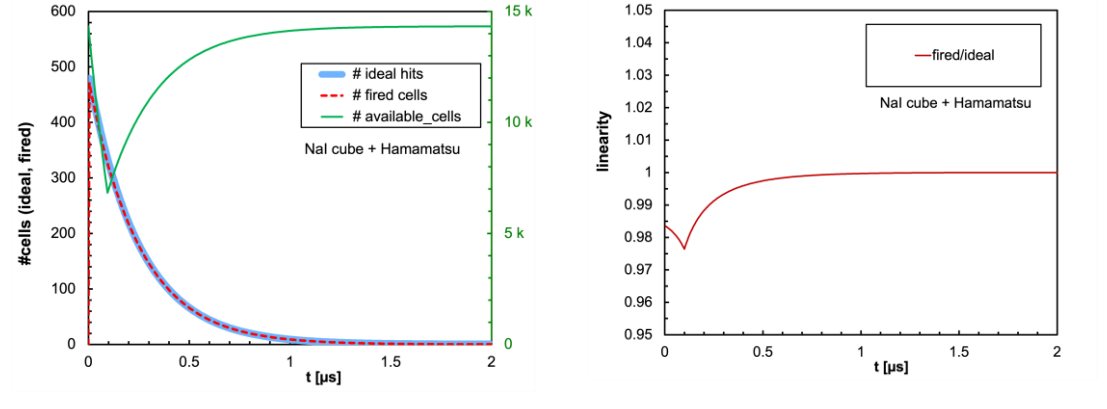

(**a**) (**b**)

 doi:10.20944/preprints202509.0685.v1

Figure 16. (**a**) Same plot as in Figure 7a with the NaI cubic crystal coupled to the Hamamatsu SiPM. (**b**) Same plot as in Figure 7b.

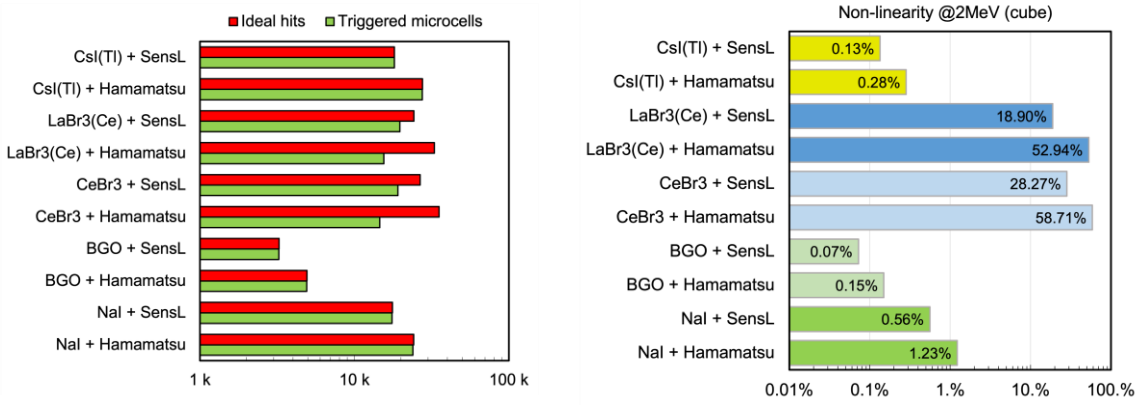

(**a**) (**b**)

Figure 17. Time-integrated results of the calculation with 2 MeV gamma energy deposited inside the five cubic scintillators. (**a**) Number of ideal hits and of actually triggered microcells for the examined configurations of scintillator and SiPM. (**b**) Expected non-linearity for each configuration.

As for the cylindrical configuration no SiPM blinding occurs, as expected due to the 16 times larger number of microcells, and as a consequence the non-linearity is much smaller in all configurations. We only show the time evolution plots for the worst case, which is the one related to the CeBr3 scintillator that has the highest light yield and the fastest decay time, in Figure 18 and Figure 19 respectively for the SensL and Hamamatsu SiPMs. Figure 20 summarizes the results for the cylindrical configurations. Then we also calculated the total number of triggered microcells as a function of the gamma energy deposited inside the scintillator for all the combinations of scintillator and SiPM listed in Table 1 and Table 2 respectively, for the two geometries of Figure 1. The resulting values are plotted in Figures 21 and 22, and are also listed in Tables A3–A6 of Appendix B. The plot of Figure 21 shows that the CsI(Tl), BGO and NaI(Tl) cubic scintillators coupled with either SiPM are expected to be linear in the full investigated energy range. A relevant nonlinearity appears instead above ≈ 1500 keV (SensL) and ≈ 900 keV (Hamamatsu) for LaBr3(Ce) and CeBr3: this represents the onset of the SiPM blinding because of the much faster decay constant of both scintillators (30 and 20 ns). These features tend to concentrate a larger number of hits in fewer microcells in a much shorter time interval. Conversely, Figure 22 shows that in the cylindrical configuration read by 16 SiPMs the behavior is basically linear with all the scintillators and both SiPMs despite the small non-linearities visible in Figure 20b.

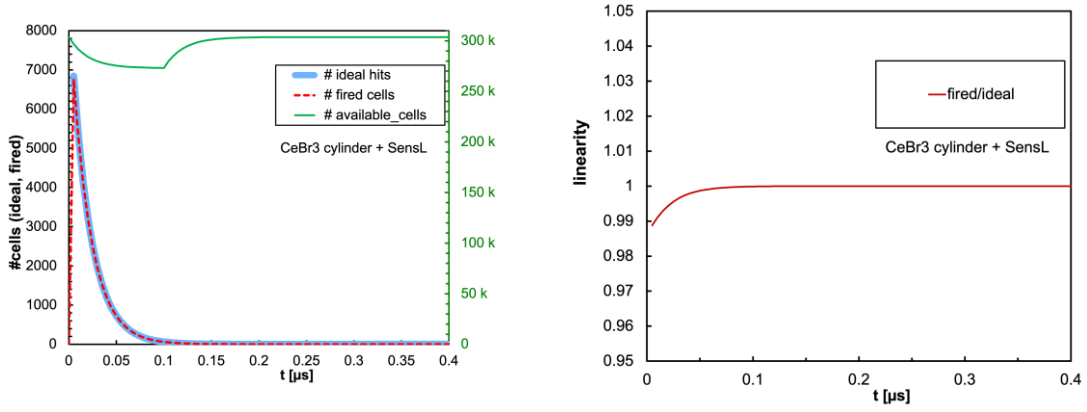

(**a**) (**b**)

 doi:10.20944/preprints202509.0685.v1

Figure 18. (**a**) Time evolution of the number of triggered (dashed red line) and of available (green line, right-hand scale) microcells, for the case of 2 MeV deposited in a 3.81 cm × 3.81 cm cylindrical CeBr3 crystal read by the SensL SiPM. The time step is 5 ns. Also shown is the ideal number of microcells (light blue line) that would be triggered if no recharge dead time were present. (**b**) Ratio between the number of fired microcells to the ideal one as a function of time.

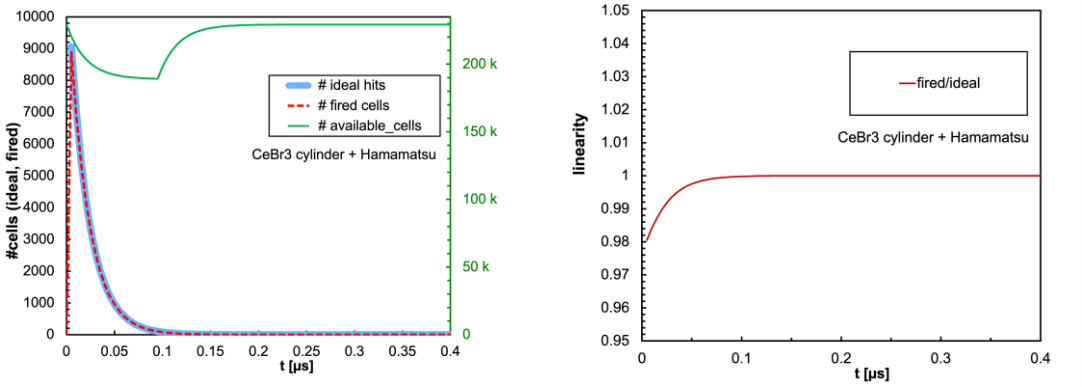

(**a**) (**b**)

Figure 19. (**a**) Same plot as in Figure 18a with the cylindrical CeBr3 crystal coupled to the Hamamatsu SiPM. (**b**) Same plot as in Figure 18b.

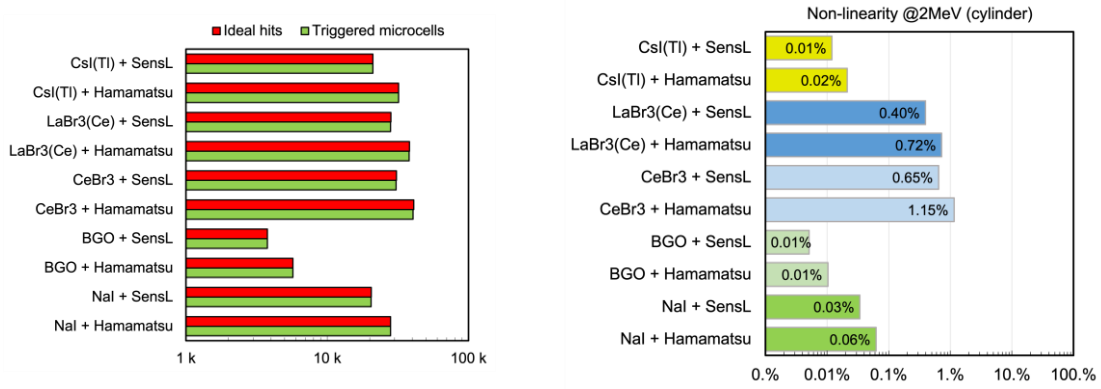

(**a**) (**b**)

Figure 20. Time-integrated results of the calculation with 2 MeV gamma energy deposited inside the five cylindrical scintillators. (**a**) Number of ideal hits and of actually triggered microcells for the examined configurations of scintillator and SiPM. (**b**) Expected non-linearity for each configuration.

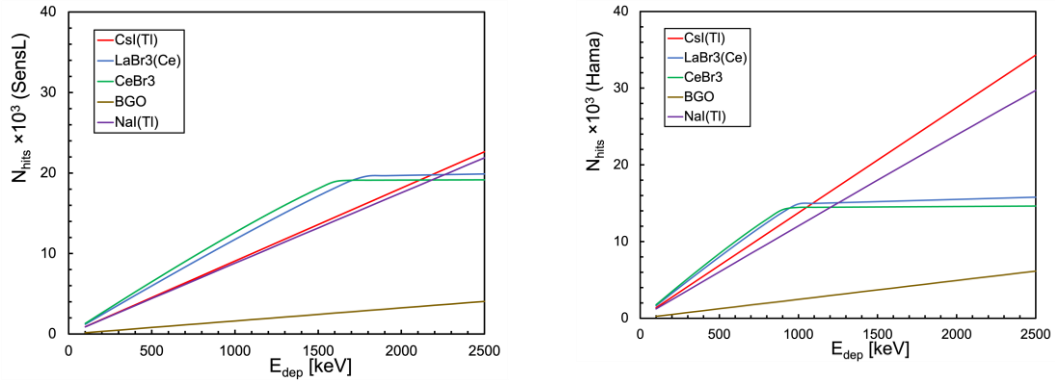

(**a**) (**b**)

 doi:10.20944/preprints202509.0685.v1

Figure 21. Calculation of the total number of triggered microcells as a function of the gamma energy deposited inside a cubic scintillator of Figure 1a. (**a**) When coupled to a SensL SiPM. (**b**) When coupled to a Hamamatsu SiPM.

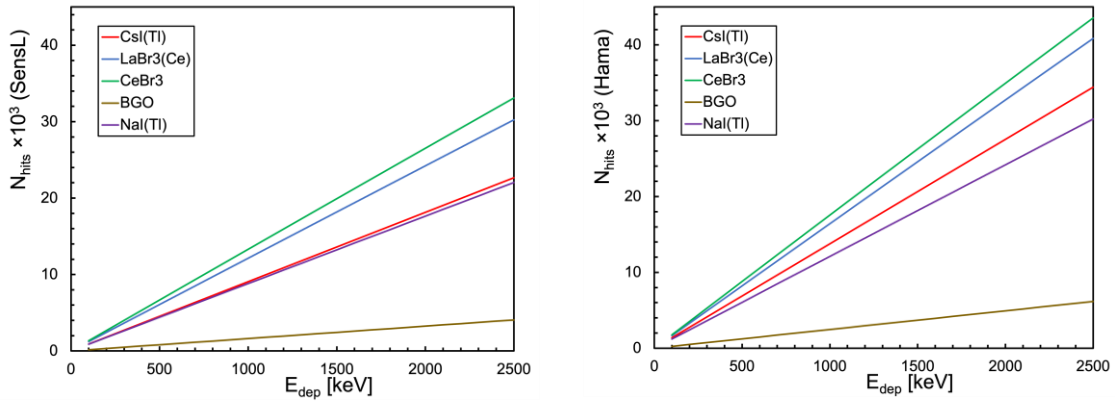

(**a**) (**b**)

Figure 22. Calculation of the total number of triggered microcells as a function of the gamma energy deposited inside a cylindrical scintillator of Figure 1b. (**a**) When coupled to an array of 16 SensL SiPMs. (**b**) When coupled to an array of 16 Hamamatsu SiPMs.

In Figure 23a and c we show two sets of spectra, taken with 1 cm × 1 cm × 1 cm CsI(Tl) crystals, read by a SensL and by a Hamamatsu SiPM respectively. Each spectrum is related to one of four gamma sources (^{226}Ra, ^{22}Na, ^{137}Cs, ^{60}Co). The data were available from previous experiments and unfortunately they were taken using different sets of sources with different activities, this is why each spectrum was normalized to its own integral. Figure 23b and d report the corresponding energy calibrations, Table 3 lists the energy values of the peaks used in the calibration for each source. The two highest energy peaks, from ^{226}Ra, were not used for the calibration but just for a linearity cross check.

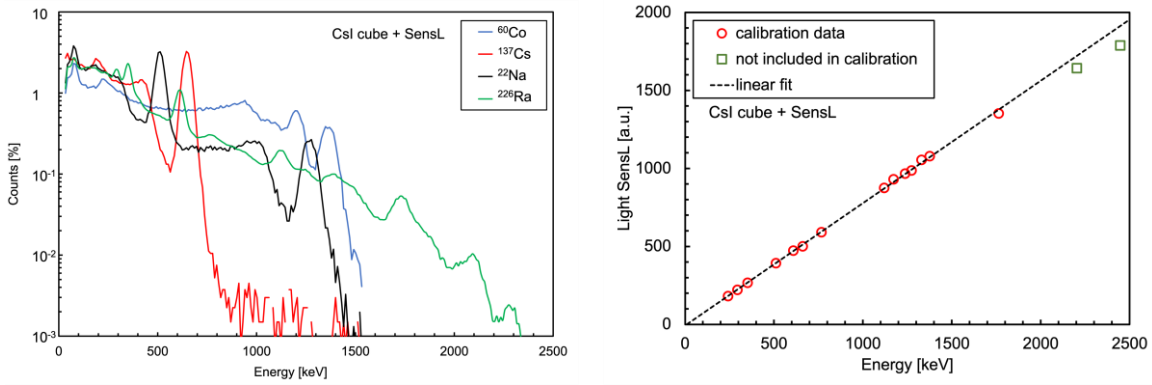

(**a**) (**b**)

 doi:10.20944/preprints202509.0685.v1

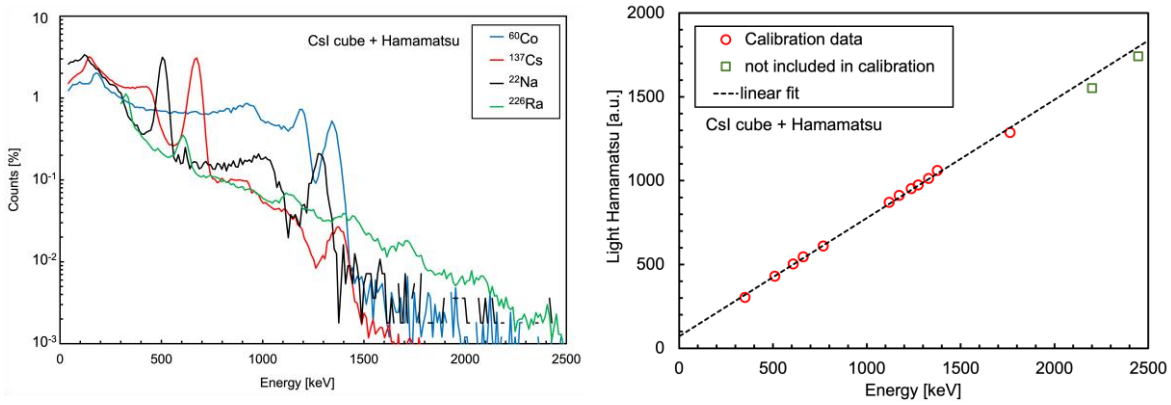

(**c**) (**d**)

Figure 23. (**a**) Spectra of four gamma sources acquired using a CsI(Tl) scintillator and a SensL SiPM. (**b**) The corresponding calibration plot. (**c**) Spectra of four gamma sources acquired using a CsI(Tl) scintillator and a Hamamatsu SiPM. (**d**) The corresponding calibration plot.

Table 3. Energy values of the peaks used in the calibration for each source. The first two were only used with the SensL equipped detector because of the large background. The two highest energy peaks from ^{226}Ra, not used for the calibration, were used as a linearity cross check.

Gamma source	Peak energy [keV]	notes
^{226}Ra	242	only used with SensL
	295	
	352	SensL and Hamamatsu
	609	
	768	
	1120	
	1238	
	1377	
	1764	
	2202	used for cross check and not for calibration
	2448	
^{137}Cs	662	SensL and Hamamatsu
^{22}Na	511	SensL and Hamamatsu
	1274	
^{60}Co	1173	SensL and Hamamatsu
	1330	

4. Discussion

The main indication from our results is that, when planning to set up a spectroscopic gamma-ray detector based on scintillator and SiPMs, careful consideration should be given both to the choice of components and to the energy range of interested. Indeed, there is a relevant interplay between the light yield of the scintillator, its decay time, the number of microcells featured by the SiPM, and the microcell recharge dead time. The SiPM, as a quasi-digital counter, has a finite number of microcells and this can give rise to a partial saturation of the output signal due to:

- Two or more photons interacting with the same microcell (multiple hit);
- A number of microcells temporarily inactive because they are recharging after being triggered.

The two effects take place massively with LaBr3 and CeBr3 scintillators, whose light emission produces a large number of photons in a very short time interval. This causes non-linearity when the deposited energy is small, but can totally blind the SiPM for a while in case of large deposited energy in the small scintillator cube (see Figures 9–12, and 21). The effect is more pronounced in the SiPM

 doi:10.20944/preprints202509.0685.v1

with a smaller number of microcells (Hamamatsu). The time-integrated non-linearities shown in Figure 17 are the result of the above mentioned interplay. In the bigger cylindrical configuration there is a relevant advantage, i.e., the number of photons produced is shared among several SiPMs so that each one sees only a fraction of them. In such a case the non-linearities are strongly reduced, as can be seen in the worst-case plots of Figures 18, 19 and 22.

If one is interested in setting up a small scintillator with a single SiPM the best candidate seems to be CsI(Tl), either using a SensL or a Hamamatsu SiPM. Indeed CsI(Tl) represents the best trade-off between linearity, energy resolution (Table 4), and chemical properties:

- LaBr3(Ce) and CeBr3, hygroscopic thus requiring an expensive air-tight case, are strongly non-linear as they blind the SiPM;
- NaI(Tl) is rather equivalent to CsI(Tl) but it is hygroscopic;
- BGO has a poor light yield, therefore the SiPM light readout would be perfectly linear but providing a poor energy resolution.
- CsI(Tl) is reasonably inexpensive as compared to LaBr3(Ce), CeBr3 and NaI(Tl), and does not require any special air-tight case thus being easy to manipulate.

Despite some claim about the possible non-linearity of similar SiPMs when detecting gamma rays above 1 MeV or less when coupled to CsI(Tl) [10], our calculations show no indication of such an effect. Indeed, Figure 23 shows a slight loss of linearity above 1.7 MeV for both the SensL and the Hamamatsu SiPMs, but this is likely to be ascribed to a non-linearity of the crystal itself, as it was also suggested in [11].

We remark that the energy resolution values quoted in Table 4 do not consider corrections for the Fano factor, and they were simply calculated as Poisson uncertainty from the number of triggered microcells (inverse square root multiplied by 2.35). However, they provide realistic indications, in particular for LaBr3(Ce) and CeBr3.

Table 4. FWHM energy resolution at 662 keV and non-linearity at 2 MeV for all the examined configurations. Notice that the resolution quoted here was naively calculated just for intercomparison as the inverse square root of the number of triggered microcells multiplied by 2.35.

		CsI(Tl)	LaBr3(Ce)	CeBr3	BGO	NaI(Tl)
SensL	Resolution @662 keV	3.03%	2.65%	2.54%	7.17%	3.08%
+ cube	Non-linearity at 2 MeV	0.13%	18.90%	28.27%	0.07%	0.56%
Hamamatsu	Resolution @662 keV	2.46%	2.30%	2.25%	5.82%	2.63%
+ cube	Non-linearity at 2 MeV	0.28%	52.94%	58.71%	0.15%	1.23%
SensL	Resolution @662 keV	3.03%	2.62%	2.50%	7.17%	3.08%
+ cylinder	Non-linearity at 2 MeV	0.01%	0.40%	0.65%	0.01%	0.03%
Hamamatsu	Resolution @662 keV	2.46%	2.25%	2.18%	5.82%	2.63%
+ cylinder	Non-linearity at 2 MeV	0.02%	0.72%	1.15%	0.01%	0.06%

As a further exercise we used our calculation method to investigate how the non-linearity evolves for bigger cubic geometries, only considering LaBr3(Ce) and CeBr3 scintillators because they are the only ones creating relevant non-linearity with SiPM readout. Therefore we evaluated the expected non-linearity at 2 MeV deposited energy for the two additional cubic configurations of Figure 24. In Table 5 we summarize the main features of these configurations along with the previously shown cubic and cylindrical ones for comparison, and in Figure 25 we compare the corresponding results which show a relevant linearity improvement and no SiPM blinding.

 doi:10.20944/preprints202509.0685.v1

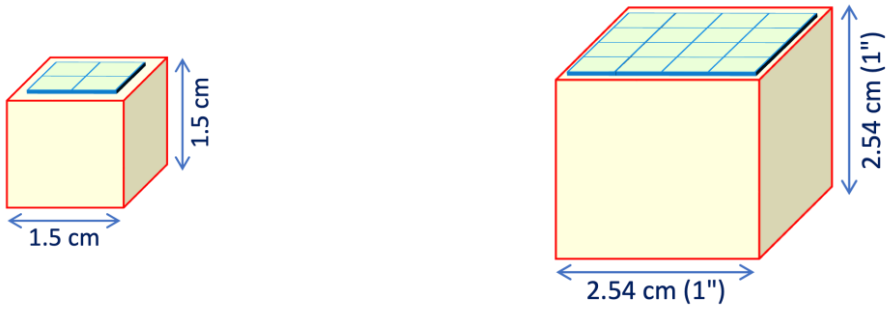

(**a**) (**b**)

Figure 24. Two additional detector geometries evaluated: (**a**) 1.5 cm × 1.5 cm × 1.5 cm scintillator coupled to a 2 × 2 array of 6 mm × 6 mm SiPMs; (**b**) 2.54 cm × 2.54 cm × 2.54 cm scintillator coupled to a 4 × 4 array of 6 mm × 6 mm SiPMs.

Table 5. Summary of the main features of the evaluated detector configurations.

	CeBr3 Hamamatsu	**LaBr3(Ce) Hamamatsu**	**CeBr3 SensL**	**LaBr3(Ce) SensL**
cube size			1 cm	
n. SiPMs			1	
n. microcells		14331		18980
sensor/total area ratio			6%	
collection efficiency			56%	
cube size			1.5 cm	
n. SiPMs			4	
n. microcells		57324		75920
sensor/total area ratio			10.7%	
collection efficiency			70%	
cube size			2.54 cm	
n. SiPMs			16	
n. microcells		229296		303680
sensor/total area ratio			14.9%	
collection efficiency			78%	
cylinder size			3.81 cm	
n. SiPMs			16	
n. microcells		229296		303680
sensor/total area ratio			8.4%	
collection efficiency			65%	

 doi:10.20944/preprints202509.0685.v1

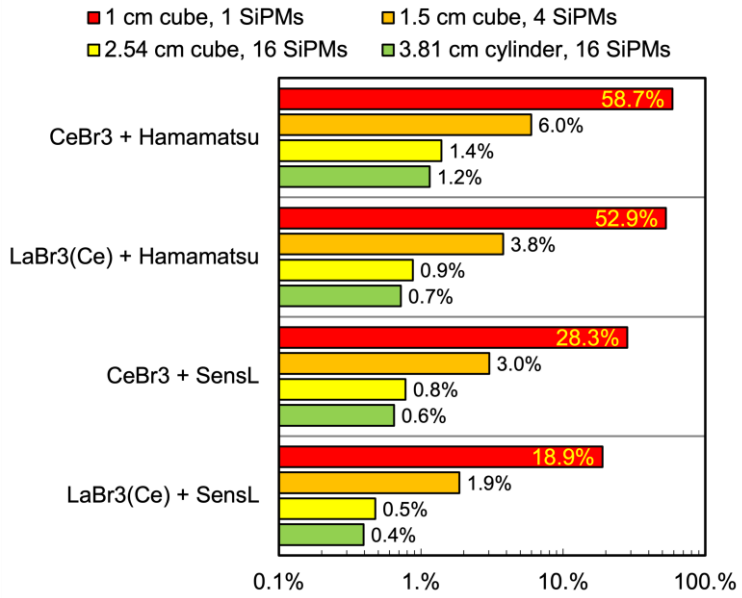

Figure 25. Expected non-linearity at 2 MeV deposited energy for four geometrical configurations of LaBr3(Ce) and CeBr3 scintillators read by different arrangements of SensL and Hamamatsu 6 mm × 6 mm SiPM arrays.

5. Conclusions

The results of our numerical analysis can likely be used when planning future radiation detection systems based on scintillators and SiPMs, as it somehow highlights their realistic linearity boundaries. The analysis also confirms the quite interesting properties of the CsI(Tl) scintillator, as it represents a good compromise between cost, performance, and ease of use, especially if planning to employ it in miniature detection systems like personal dosimeters. For higher level spectroscopic applications of scintillators the feasibility of larger cylindrical configurations, coupled to arrays of SiPMs, has been confirmed up to a few MeV. LaBr3(Ce) and CeBr3 are the best options in terms of timing and energy resolution, even though CsI(Tl) remains a notable candidate as well.

Supplementary Materials: The following supporting files have been submitted along with this manuscript: time_evolution_cube.xlsx, time_evolution_cyl.xlsx

Author Contributions: Conceptualization, P.F., C.R.F., S.A. and G.E.P.; methodology, P.F., C.R.F., S.A. and G.E.P.; software, P.F. and S.A.; validation, P.F., C.R.F., S.A. and G.E.P.; formal analysis, P.F.; investigation, P.F. and S.A.; resources, P.F.; data curation, P.F., C.R.F., S.A. and G.E.P.; writing—original draft preparation, P.F.; writing—review and editing, P.F., C.R.F., S.A. and G.E.P.; visualization, P.F.; supervision, P.F.; project administration, P.F.; funding acquisition, P.F. All authors have read and agreed to the published version of the manuscript.

Funding: S. Amaducci was supported by PNRR SAMOTHRACE - codice ecs00000022 - cup I63C21000320006 - M4 - C2 - inv. 1.5 - avviso n. 3277 del 30-12-2021.

Data Availability Statement: The following supporting files have been submitted along with this manuscript: time_evolution_cube.xlsx, time_evolution_cyl.xlsx

Conflicts of Interest: The authors declare no conflicts of interest.

 doi:10.20944/preprints202509.0685.v1

Appendix A

Table A1. Cube configuration: light collection efficiency results from Geant4 simulation, from our simple model and from the simple model with increased Ɛ value (these data are plotted on Figure 2a and Figure 3a).

reflectivity	Geant4	simple model	simple/Geant4	Ɛ+ model	Ɛ+/Geant4
0.9	40.8%	39.0%	0.95	40.6%	0.99
0.91	43.6%	41.5%	0.95	43.2%	0.99
0.92	46.1%	44.4%	0.96	46.1%	1.00
0.93	49.1%	47.7%	0.97	49.4%	1.01
0.94	53.1%	51.5%	0.97	53.3%	1.00
0.95	57.9%	56.1%	0.97	57.8%	1.00
0.96	62.8%	61.5%	0.98	63.1%	1.00
0.97	69.4%	68.0%	0.98	69.5%	1.00
0.98	77.0%	76.1%	0.99	77.4%	1.00
0.99	87.0%	86.5%	0.99	87.2%	1.00
1	100.0%	100.0%	1.00	100.0%	1.00

Table A2. Cylinder configuration: light collection efficiency results from Geant4 simulation, from our simple model and from the simple model with increased Ɛ value (these data are plotted on Figure 2b and Figure 3b).

reflectivity	Geant4	simple model	simple/Geant4	Ɛ+ model	Ɛ+/Geant4
0.9	49.5%	47.9%	0.97	49.7%	1.00
0.91	52.5%	50.5%	0.96	52.3%	1.00
0.92	55.4%	53.5%	0.97	55.2%	1.00
0.93	58.3%	56.8%	0.97	58.5%	1.00
0.94	62.0%	60.5%	0.98	62.2%	1.00
0.95	66.3%	64.8%	0.98	66.4%	1.00
0.96	71.2%	69.7%	0.98	71.2%	1.00
0.97	76.6%	75.4%	0.98	76.7%	1.00
0.98	83.1%	82.1%	0.99	83.1%	1.00
0.99	90.7%	90.2%	0.99	90.8%	1.00
1	100.0%	100.0%	1.00	100.0%	1.00

Appendix B

Table A3. Number of triggered microcells as a function of deposited gamma energy for the cubic configuration of Figure 1a with the SensL SiPM (data plotted in Figure 21a).

Edep [keV]	CsI(Tl)	LaBr3(Ce)	CeBr3	BGO	NaI(Tl)
100	907	1212	1327	162	882
200	1814	2417	2642	325	1763
300	2721	3615	3944	487	2644
400	3628	4805	5232	650	3525
500	4534	5988	6506	812	4405
600	5441	7162	7765	974	5284
700	6347	8326	9008	1137	6163
800	7254	9481	10233	1299	7042
900	8160	10624	11439	1461	7920
1000	9066	11755	12622	1623	8798
1100	9972	12873	13782	1786	9675
1200	10878	13975	14913	1948	10551
1300	11783	15059	16010	2110	11427
1400	12689	16121	17063	2272	12303

 doi:10.20944/preprints202509.0685.v1

1500	13594	17153	18055	2435	13177
1600	14500	18145	18926	2597	14051
1700	15405	19064	19099	2759	14925
1800	16310	19637	19106	2921	15798
1900	17215	19674	19113	3083	16670
2000	18120	19710	19120	3246	17541
2100	19024	19747	19127	3408	18412
2200	19929	19783	19134	3570	19282
2300	20833	19820	19141	3732	20151
2400	21737	19856	19148	3894	21019
2500	22641	19893	19155	4056	21887

Table A4. Number of triggered microcells as a function of deposited gamma energy for the cubic configuration of Figure 1a with the Hamamatsu SiPM (data plotted in Figure 21b).

Edep [keV]	CsI(Tl)	LaBr3(Ce)	CeBr3	BGO	NaI(Tl)
100	1377	1638	1750	246	1209
200	2754	3259	3471	493	2417
300	4131	4861	5160	739	3624
400	5507	6442	6812	985	4830
500	6883	7998	8424	1232	6034
600	8259	9524	9986	1478	7238
700	9634	11013	11487	1724	8439
800	11009	12452	12902	1970	9640
900	12383	13811	14159	2216	10839
1000	13758	14901	14449	2462	12036
1100	15131	14973	14461	2708	13232
1200	16504	15032	14473	2954	14426
1300	17877	15090	14485	3200	15618
1400	19249	15148	14497	3446	16808
1500	20621	15207	14508	3692	17996
1600	21993	15265	14521	3938	19181
1700	23364	15323	14533	4184	20364
1800	24734	15381	14544	4429	21544
1900	26104	15440	14556	4675	22721
2000	27474	15497	14568	4921	23896
2100	28843	15556	14580	5166	25066
2200	30211	15614	14592	5412	26233
2300	31579	15673	14604	5657	27396
2400	32947	15731	14616	5903	28554
2500	34314	15789	14628	6148	29707

Table A5. Number of triggered microcells as a function of deposited gamma energy for the cylindrical configuration of Figure 1b with the SensL SiPM (data plotted in Figure 22a).

Edep [keV]	CsI(Tl)	LaBr3(Ce)	CeBr3	BGO	NaI(Tl)
100	907	1215	1332	162	882
200	1814	2430	2664	325	1764
300	2721	3644	3995	487	2646
400	3629	4858	5325	650	3528
500	4536	6071	6655	812	4410
600	5443	7284	7984	974	5292
700	6350	8496	9312	1137	6173
800	7257	9709	10639	1299	7055

 doi:10.20944/preprints202509.0685.v1

900	8164	10920	11966	1462	7937
1000	9071	12132	13291	1624	8819
1100	9978	13342	14616	1786	9700
1200	10886	14553	15941	1949	10582
1300	11793	15763	17264	2111	11464
1400	12700	16973	18587	2274	12345
1500	13607	18182	19909	2436	13227
1600	14514	19391	21230	2598	14109
1700	15421	20599	22551	2761	14990
1800	16328	21807	23871	2923	15872
1900	17235	23014	25190	3085	16753
2000	18142	24222	26508	3248	17635
2100	19049	25428	27825	3410	18516
2200	19956	26634	29142	3573	19398
2300	20863	27840	30458	3735	20279
2400	21770	29046	31773	3897	21161
2500	22677	30250	33087	4060	22042

Table A6. Number of triggered microcells as a function of deposited gamma energy for the cylindrical configuration of Figure 1b with the SensL SiPM (data plotted in Figure 22b).

Edep [keV]	CsI(Tl)	LaBr3(Ce)	CeBr3	BGO	NaI(Tl)
100	1378	1646	1763	246	1210
200	2755	3291	3525	493	2419
300	4133	4935	5284	739	3629
400	5510	6578	7042	986	4838
500	6888	8220	8799	1232	6047
600	8265	9861	10553	1478	7256
700	9642	11500	12306	1725	8466
800	11020	13139	14057	1971	9675
900	12397	14777	15807	2218	10884
1000	13775	16414	17554	2464	12093
1100	15152	18050	19300	2710	13302
1200	16529	19685	21044	2957	14511
1300	17906	21318	22786	3203	15719
1400	19284	22951	24527	3449	16928
1500	20661	24582	26266	3696	18137
1600	22038	26213	28002	3942	19345
1700	23415	27842	29737	4188	20554
1800	24793	29471	31471	4435	21762
1900	26170	31098	33202	4681	22971
2000	27547	32724	34931	4928	24179
2100	28924	34349	36659	5174	25387
2200	30301	35973	38385	5420	26595
2300	31678	37596	40109	5667	27804
2400	33055	39218	41830	5913	29012
2500	34432	40838	43550	6159	30220

References

1. Fourches, N.; Zielińska, M.; Charles, G. High Purity Germanium: From Gamma-Ray Detection to Dark Matter Subterranean Detectors. In *Use of Gamma Radiation Techniques in Peaceful Applications*; IntechOpen: London, UK, 2019; pp. 1–17. https://doi.org/10.5772/intechopen.78481.

 doi:10.20944/preprints202509.0685.v1

2. McGregor, D.S. Materials for Gamma-Ray Spectrometers: Inorganic Scintillators. *Annu. Rev. Mater. Res.* **2018**, *48*, 245.
3. Derenzo, S.E.; Weber, M.J.; Bourret-Courchesne, E.; Klintenberg, M.K. The quest for the ideal inorganic scintillator. *Nucl. Instrum. Methods Phys. Res. Sect. A* **2003**, *505*, 111–117.
4. Finocchiaro, P.; Pappalardo, A.; Cosentino, L.; Belluso, M.; Billotta, S.; Bonanno, G.; Carbone, B.; Condorelli, G.; Di Mauro, S.; Fallica, G.; et al. Characterization of a Novel 100-Channel Silicon Photomultiplier—Part I: Noise. *IEEE Trans. Electron Devices* **2008**, *55*, 2757–2764.
5. Finocchiaro, P.; Pappalardo, A.; Cosentino, L.; Belluso, M.; Billotta, S.; Bonanno, G.; Carbone, B.; Condorelli, G.; Di Mauro, S.; Fallica, G.; et al. Characterization of a Novel 100-Channel Silicon Photomultiplier—Part II: Charge and Time. *IEEE Trans. Electron Devices* **2008**, *55*, 2765–2773.
6. Finocchiaro, P.; Pappalardo, A.; Cosentino, L.; Belluso, M.; Billotta, S.; Bonanno, G.; Di Mauro, S. Features of Silicon Photo Multipliers: Precision Measurements of Noise, Cross-Talk, Afterpulsing, Detection Efficiency. *IEEE Trans. Nucl. Sci.* **2009**, *56*, 1033.
7. Bonanno, G.; Finocchiaro, P.; Pappalardo, A.; Billotta, S.; Cosentino, L.; Belluso, M.; Di Mauro, S.; Occhipinti, G. Precision measurements of Photon Detection Efficiency for SiPM detectors. *Nucl. Instrum. Methods Phys. Res. Sect. A* **2009**, *610*, 93–97.
8. Swiderski, L.; Moszyński, M.; Czarnacki, W.; Brylew, K.; Grodzicka-Kobylka, M.; Mianowska, Z.; Sworobowicz, T.; Syntfeld-Każuch, A.; Szczesniak, T.; Klamra, W.; et al. Scintillation response to gamma-rays measured at wide temperature range for Tl doped CsI with SiPM readout. *Nucl. Instrum. Methods Phys. Res. Sect. A* **2019**, *916*, 32–36.
9. Grodzicka, M.; Moszynski, M.; Szczesniak, T.; Kapusta, M.; Szawłowski, M.; Wolski, D. Energy resolution of small scintillation detectors with SiPM light readout. *JINST* **2013**, *8*, P02017.
10. Grodzicka-Kobylka, M.; Szczesniak, T.; Moszyński, M. Comparison of SensL and Hamamatsu 4×4 channel SiPM arrays in gamma spectrometry with scintillators. *Nucl. Instrum. Methods Phys. Res. Sect. A* **2017**, *856*, 53–64.
11. Mianowska, Z.; Moszynski, Z.M.; Brylew, K.; Chabera, M.; Dziedzic, A.; Gektin, A.V.; Krakowski, T.; Mianowski, S.; Syntfeld-Każuch, A.; Szczesniak, T.; et al. The light response of CsI:Tl crystal after interaction with gamma radiation study using analysis of single scintillation pulses and digital oscilloscope readout. *Nucl. Instrum. Methods Phys. Res. Sect. A* **2022**, *1031*, 166600.
12. Rossi, F.; Cosentino, L.; Longhitano, F.; Minutoli, S.; Musico, P.; Osipenko, M.; Poma, G.E.; Ripani, M.; Finocchiaro, P. The Gamma and Neutron Sensor System for Rapid Dose Rate Mapping in the CLEANDEM Project. *Sensors* **2023**, *23*, 4210. https://doi.org/10.3390/ s23094210.
13. Poma, G.E.; Failla, C.R.; Amaducci, S.; Cosentino, L.; Longhitano, F.; Vecchio, G.; Finocchiaro, P. PI3SO: A Spectroscopic Gamma-Ray Scanner Table for Sort and Segregate Radwaste Analysis. *Inventions* **2024**,*9*,85. https:// doi.org/10.3390/inventions9040085.
14. Ripani, M.; Rossi, F.; Cosentino, L.; Longhitano, F.; Musico, P.; Osipenko, M.; Poma, G.E.; Finocchiaro, P. Field Test of the MiniRadMeter Gamma and Neutron Detector for the EU Project CLEANDEM. *Sensors* **2024**, *24*, 5905. https://doi.org/10.3390/s24185905.
15. Longhitano, F.; Poma, G.E.; Cosentino, L.; Finocchiaro, P. A Scintillator Array Table with Spectroscopic Features. *Sensors* **2022**, *22*, 4754. https://doi.org/10.3390/s22134754.
16. Berkeley Lab inorganic scintillator library. Available online: https://scintillator.lbl.gov/inorganic-scintillator-library/ (accessed on 3 August 2025).
17. MicroFC-60035-SMT. Available online: https://www.onsemi.com/pdf/datasheet/microc-series-d.pdf (accessed on 4 August 2025).
18. S14160-6050HS. Available online: https://www.hamamatsu.com/content/dam/hamamatsu-photonics/sites/documents/99_SALES_LIBRARY/ssd/s14160_s14161_series_kapd1064e.pdf (accessed on 4 August 2025).
19. Shahmaleki, S.; Rahmani, F. Scintillation properties of CsI(Tl) co-doped with Tm2+. *Radiation Physics and Engineering* **2021**, *2(2):13–19*. https://doi.org/10.22034/rpe.2021.295907.1032
20. van Dam, H.T.; Seifert, S.; Drozdowski, W.; Dorenbos, P.; R. Schaart, D.R. Optical Absorption Length, Scattering Length, and Refractive Index of LaBr3:Ce3+. *IEEE Trans. Nucl. Sci*., **2012**, v59, n3, 656.

 doi:10.20944/preprints202509.0685.v1

21. Drozdowski, W.; Dorenbos, P.; Bos, A.J.J.; Bizarri, G.; Owens, A.; Quarati, F.G.A. CeBr3 Scintillator Development for Possible Use in Space Missions. *IEEE Trans. Nucl. Sci.*, **2008**, v55, n3, 1391.
22. Mehrdel, B.; Kratochwil, N.; Seo, Y.; Glodo, J.; Bhattacharya, P.; Ariño-Estrada, G.; Caravaca, J. Enhancing the Cherenkov over scintillation ratio using dichroic filters in BGO and TlCl for TOF-PET. *Scientific Reports* **2025**, 15,18731. https://doi.org/10.1038/s41598-025-01396-2.
23. Tapan, I.; Kocak, F. New Crystal Photodiode Combination for Environmental Radiation Measurement. *Journal of Advanced Applied Sciences* **2023**, 2(2), 64. https://doi.org/10.61326/jaasci.v2i2.103.
24. Agostinelli, S.; Allison, J.; Amako, K.; Apostolakis, J.; Araujo, H.; Arce, P.; Asai, M.; Axen, D.; Banerjee, S.; Barrand, G.; et al. Geant4—A simulation toolkit. *Nucl. Instrum. Methods Phys. Res. Sect. A* **2003**, *506*, 250–303.
25. Lambertian Surface. Available online: https://phys.libretexts.org/Bookshelves/Astronomy__Cosmology/Stellar_Atmospheres_(Tatum)/01%3A_Definitions_of_and_Relations_between_Quantities_used_in_Radiation_Theory/1.13%3A_Lambertian_Surface (accessed on 11 August 2025).